Journal Name

ARTICLE

Rapid flame synthesis of internal Mo^{6+} doped TiO$_2$ nanocrystals *in-situ* decorated with highly dispersed MoO$_3$ clusters for lithium ion storage

Yunfeng Li,[a,b] Yanjie Hu,[a,]* Jianhua Shen,[a] Haibo Jiang,[a] Guoquan Min,[b,]* Shengjie Qiu,[b] Zhitang Song,[c] Zhuo Sun,[d] and Chunzhong Li[a,]*

Rational design of nanoheterostructured materials has attracted much attention because of its importance for developing highly efficient LIBs. Herein, we have demonstrated the internal Mo^{6+} doped TiO$_2$ nanocrystals *in-situ* decorated with highly dispersed MoO$_3$ clusters have been realized by a facile and rapid flame spray pyrolysis route for electrochemical energy storage. In such intriguing nanostructures, internal Mo^{6+} doping can improve the conductivity of electrode materials and facilitate rapid Li$^+$ intercalation and ion transport and the heteroassembly of highly dispersed ultrafine MoO$_3$ clusters with excellent electrochemical activity endows the TiO$_2$ with extra Li$^+$ ions storage ability as well as the Mo^{6+} incorporated. Thus, as-prepared nanohybrids electrodes exhibit a high specific capacity and superior rate capability due to the maximum synergetic effect of TiO$_2$, Mo^{6+} and ultrafine MoO$_3$ clusters. Moreover, aerosol flame process with unique temperature gradient opens a new strategy to design novel hybrid materials by the simultaneous doping and heteroassembly engineering for next-generation LIBs.

Introduction

Rechargeable lithium-ion batteries (LIBs), as powerful and green energy storage devices, have demonstrated their significant roles in portable electronic devices and hybrid electric vehicles (HEVs) due to high storage capacities and power densities, long cycle life, and environment benignity.[1-4] Rational design of advanced electrode materials are extremely important for developing highly efficient LIBs. Compared to graphite with low operating voltage (below 0.2 V *vs.* Li/Li$^+$), titanium oxide (TiO$_2$) possesses a better safety because of its low volume change (~ 3 %) and the relative high lithium insertion/extraction voltage (higher than 1.75 V *vs.* Li/Li$^+$) for LIBs.[5-7] In addition, with the advantages of low-cost, safety, and environmentally benign feature, TiO$_2$ have been considered as a promising alternative anode materials.[8-10] However, TiO$_2$ as anode materials still suffer either intrinsically poor electrical conductivity

[a] *Key Laboratory for Ultrafine Materials of Ministry of Education, School of Materials Science and Engineering, East China University of Science & Technology, Shanghai 200237, China. Email: czli@ecust.edu.cn; huyanjie@ecust.edu.cn; Fax: +86 21 64250624; Tel: +86 21 6425 0949*
[b] *Shanghai Nanotechnology Promotion Center, Shanghai 200237, China. Email:guoquan@snpc.org.cn*
[c] *Shanghai Institute of Micro-system and information Technology, Chinese Academy of Sciences, Shanghai 200050, China*
[d] *Department of Physics, East China Normal University, Shanghai 200062, China†*
†*Electronic Supplementary Information (ESI) available:* SEM, TEM images, XRD patterns, EDX and the discharge-charge capacity of the Mo^{6+}-TiO$_2$/MoO$_3$ NHs, TiO$_2$, and the Mo^{6+}-TiO$_2$/MoO$_3$ NHs after the sulfuration, and Nitrogen adsorption/desorption isotherms of the Mo^{6+}-TiO$_2$/MoO$_3$ NHs. See DOI: 10.1039/x0xx00000x

(~ 10^{-12} Ω^{-1} cm^{-1}) or low specific capacity, which extremely limit its practical application in LIBs.[11-12]

To improve the conductivity of TiO$_2$ electrodes, recent significant advances have focused on engineered incorporation of heteroatoms to alter the electronic structure of TiO$_2$ nanocrystals, similar effect in doped photocatalysts.[13-17] Anatase TiO$_2$ nanocrystals codoped with N and S atoms showed a superior high rate ability (63.5 mA h g^{-1} at a current density of 1.68 A g^{-1}) due to remarkably lowered electronic resistance.[18] Usui et al. found that the Ti$_{0.94}$Nb$_{0.06}$O$_2$ electrode showed a high reversible capacity of 120 mA h g^{-1} even at a high current density of 16.75 A g^{-1} because of higher conductivity from Nb doping.[19] Nevertheless, a small theoretical capacity of ~ 170 mA h g^{-1} is difficult to afford the demands for LIBs with high energy density and power density. Recently, oxides nanocrystals with high electrochemical acitivity (i.e., SnO$_2$: ~ 790 mA h g^{-1} , MoO$_3$: ~ 1111 mA h g^{-1}) have coupled with stable TiO$_2$ for achieving superior performance.[20-22] Yu et al. have demonstrated that 5 at.% Sn modified TiO$_2$ nanotube exhibited a highly specific capacity of 386 mA h g^{-1} at 0.1 C after 50 cycles.[23] Similar stable capacity of 485 mA h g^{-1} at 50 mA g^{-1} is delivered for SnO$_2$/TiO$_2$.[24] Zhang et al. reported that hydrothermal synthesized MoO$_3$/TiO$_2$ nanocomposites displayed a high reversible capacity of 408 mA h g^{-1} at 60 mA g^{-1} after 200 cycles.[25] These results suggest that high electrochemcial active oxides crystals engineered into TiO$_2$ electrode provide the best opportunity for high LIBs capacity due to their synergetic effect. However, owing to the easily phase separation and mismatch of crystals growth, highly efficient coupling TiO$_2$ with high active components with the maximized atomic interaction at nanoscale is still a great challenge for energy storage.

Flame synthesis have already been demonstrated to a versatile one-step route for synthesizing advanced nanomaterials, especially for homogeneous internal heteroatioms doping (Fe, V, Ta, N) into TiO_2 with the flame spray pyrolysis (FSP) process.[26-32] Recently, we reported double faced γ-Fe_2O_3||SiO_2 and core-shell α-Fe_2O_3/SnO_2 heterostructures by a simple flame process and found that both the ions doping and the interfacial, phase-segregation growth of second oxides species could be realized because of high-temperature reaction and unique temperature gradient profiles.[30, 31] Herein, internal Mo^{6+} doped TiO_2 nanocrystals *in-situ* decorated with highly dispersed MoO_3 clusters nanohybrids (denoted as Mo^{6+}-TiO_2/MoO_3 NHs) have been realized by an aerosol flame spray pyrolysis route, which results in the formation of novel, quasi-chain Mo^{6+}-TiO_2/MoO_3 NHs. In such intriguing nanostructures, internal Mo^{6+} doping can improve the conductivity for facilitated Li^+ intercalation and ion transport. And the heteroassembly of highly dispersed ultrafine MoO_3 clusters with excellent electrochemical activity endows the TiO_2 with extra Li^+ ions storage spaces as well as the Mo^{6+} incorporated through the conversion reaction with Li^+ ions. Thus, as-prepared Mo^{6+}-TiO_2/MoO_3 NHs as anode exhibits a high discharge capacity and superior rate capability due to the maximum synergetic effect of TiO_2, Mo^{6+} and ultrafine MoO_3 clusters at nanoscale.

Experimental

Flame Synthesis of Mo^{6+}-TiO_2/MoO_3 NHs.

The Mo^{6+}-TiO_2/MoO_3 NHs were synthesized by a facile flame spray pyrolysis route with high temperature process, described in our previous work[30-32] and the corresponding schematic setup is shown **Fig. 1**. In brief, the xylene solution (0.5 M) of titanium tetrabutoxide (99 %, Lingfeng Chemical reagent Co., Ltd., China) and acetyl acetone molybdenum (99 %, Adamas reagent Co., Ltd.) was sprayed out from the external gas assisted nozzle (dispersed O_2: 5 L min^{-1}, nozzle pressure: 0.15 MPa) to form a fine droplet. The feeding rate is fixed at a 5 mL min^{-1}. Then the spray was ignited by a ring shaped, inverse H_2/O_2 diffusion flame (H_2: 6.33 L min^{-1}, O_2: 16.67 L min^{-1}). Owing to high temperature and rapid quenching rate, targeted materials are formed and the product stream was drawn from combustion chamber and collected on the glass fiber filters (ADVTECH/GA55, Japan) by vacuum pump. The designed concentration of molybdenum was varied from 0, 1, 5, 10, and 15 % (molar ratio with respect to Ti).

Materials Characterization.

The phase composition was identified with X-ray diffraction (XRD) (a Rigaku D/max 2550VB/PC diffractometer) at room temperature. The patterns were recorded over the angular range 10-80° (2θ) with a step of 0.02° using Cu Kα radiation (λ = 0.154056 nm) and the working voltage and current are fixed at 40 kV and 100 mA, respectively. The morphologies were identified by high resolution electron microscopy (HRTEM: JEOL-2100) and filed emission scanning electron microscopy (FE-SEM: HIACHI-S4800) with energy dispersive X-ray spectroscopy (EDX). X-ray photoelectron spectroscopy (XPS) were measured by a Thermo Fisher ESCALAB 25 to determine the effect of Mo doped into the TiO_2 lattice and surface chemical states of Ti, Mo, and O. The Mo/Ti molar ratio was further measured by inductive coupled plasma emission spectrometer (ICP, Agilent 725ES, USA Thermo Elemental). The corresponding UV-vis spectra was checked by an UV-vis spectrophotometer (Cary-500 spectrometer, Varian Ltd.). Nitrogen adsorption-desorption (Micromeritics ASAP 2460 version 2.01) was determined by the Brunauer-Emmett-Teller (BET) method.

Electrochemical Evaluation.

The working electrode was composed of 80 % active materials (flame sprayed NAs), 10 % conductive material (acetylene black, AB) and 10 % binder (polyvinyldifluoride, PVDF).[21, 31] These components were mixed and stirred into slurry with N-methyl-2-pyrrolidone (NMP) and uniformly pasted on Cu foils (19 μm) with a membrane thickness of 50 μm. The average loading mass of active materials have an average value of 0.52 mg/cm^2 (the area of used Cu foils is 1.44 cm^2). Thin lithium metal foils (φ 16 × 1.2 mm) and polypropylene (PP) membrane (Celgard 2400) were employed as the counter electrode and separator, respectively. 1 M $LiPF_6$ dissolved in ethylene carbonate/diethyl carbonate (EC-DEC, 1:1 w/w) was used as the electrolyte. The half-cells (CR2016 coin type) were assembled in a argon with a high purity filled glove box (Mikrouna Advanced Series), where moisture and oxygen levels were controlled under 1 ppm. Cyclic voltammograms (CV) and electrochemical impedance spectroscopy (EIS) of the working electrode were measured by electrochemical workstation (Autolab PGSTAT302N). A LAND-CT2001C test system was used to measure galvanostatic cycle performance of cells at different current densities (from 0.1 A g^{-1} to 2 A g^{-1}) in the voltage range from 0.01 V to 3.0 V.
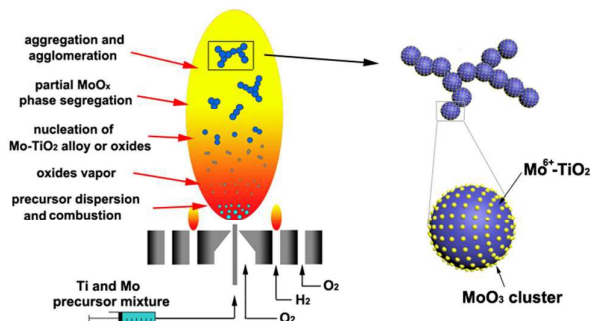

Fig. 1 Illustration of the formation of the Mo^{6+}-TiO_2/MoO_3 NHs in a rapid spray flame process.

Results and discussion

Morphology and Composition.

Novel Mo^{6+}-TiO_2/MoO_3 NHs have been fabricated by a facile flame spray pyrolysis of precursor solution containing Ti and Mo species. Being a bottom-up route, it is effective for preparing highly crystalline particles by a gas-to-particle conversion reaction. **Fig. 1** shows the illustrated formation process of Mo^{6+}-TiO_2/MoO_3 NHs. Firstly, the designed precursor in xylene was delivered in to a special nozzle assisted by an external O_2 and sprayed into fine droplets. These fuel & precursor droplets were ignited with a assist of an inverse H_2/O_2 diffusion flame and underwent evaporation, combustion, decomposition and oxidation to form uniform aerosol

TiO_x and MoO_x species by high-temperature gas reaction. Subsequently, the Ti and Mo oxides species are converted into nanoclusters by nucleation and growth. Owing to rapid decrease of temperature (- 170 °C/cm along the flame axis) by radiation and convection,[33] some Mo^{6+} ions was incorporated into the lattices of fresh TiO_2 particles to form the internal heteroatoms doping. However, because of larger ionic radium of Mo^{6+} (0.068 nm) than that of Ti^{4+} (0.0605 nm),[22, 25] some MoO_3 species can nucleate and grow on the surface of TiO_2 particles to form heterojunctions clusters because of diffusion arrangement and phase-segregation induced growth.[30,31] Meanwhile, quasi-chain aggregates and agglomerates (i.e., chain-like fumed silica) were obtained because of the hindered growth of particles derived from rapidly cooling of flame temperature.
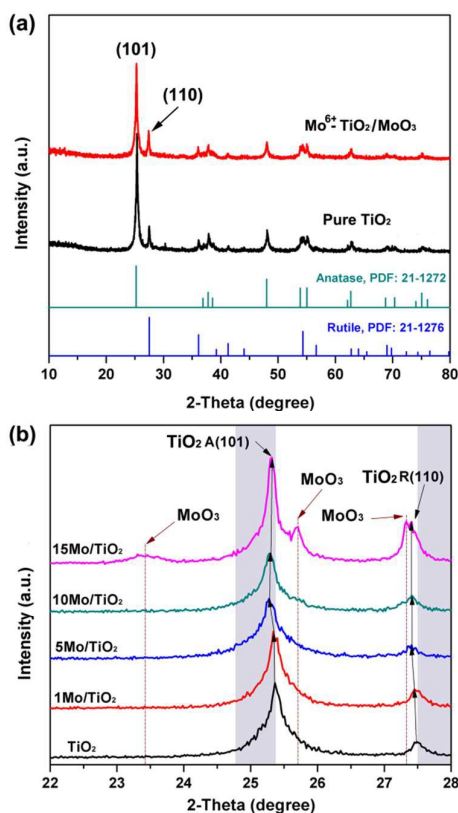

Fig. 2 (a) XRD profiles of as-prepared Mo^{6+}-TiO_2/MoO_3 NHs and pristine TiO_2 particles, (b) the enlarged XRD patterns at 22 - 28° of flame made TiO_2 with different Mo content.

Fig. 2a shows the XRD patterns of as-prepared Mo^{6+}-TiO_2/MoO_3 NHs and pristine TiO_2 particles. Clearly, it can be seen that both samples have bicrystalline phase TiO_2: anatase (JCPDS, No. 21-1272) and rutile (JCPDS, No. 21-1276), which is in agreement with the reported TiO_2 particles in flame.[26-29] The phase contents of anatase and rutile in the samples are obtained from the peak intensities of anatase (101) and rutile (110), and the calculated rutile values 22.3%, 23.2%, 22.6%, 22.9% and 23.0% for flame made TiO_2 with x % Mo (x=1, 5, 10, and 15), respectively. That's to say, the introduction of Mo species do not cause the phase conversion of anatase to rutile, which is different from the effect of Fe and Cr atoms.[26, 28] Further, no apparent peaks of MoO_3 oxides can been

identified in the XRD pattern of Mo^{6+}-TiO_2/MoO_3 NHs except a weak peak at 2θ = 25.70°, indicating that Mo is incorporated into the internal lattice of TiO_2, or MoO_3 with small size is highly dispersed. **Fig. 2b** displays the effect of Mo content on the phase composition of flame made TiO_2 particles. Clearly, with the increase of Mo content, the diffraction peaks of anatase (101) (2θ = 25.36°) shift to lower angles of 25.33°, 25.28°, 25.28° and 25.29°, respectively and the diffraction angles (2θ) of rutile (110) exhibit a simultaneous decrease from 27.49° to 27.47°, 27.42°, 27.42° and 27.41°, respectively. The maximum angle shifts of 0.08° and 0.07° are identified for anatase and rutile, respectively. This shift suggests that lattice parameter of TiO_2 is enlarged slightly with the increase of Mo ions ratios derives from larger ionic radius of Mo^{6+} (0.068 nm). Interestingly, when the content of Mo exceed 5 %, there is no change of the diffraction angle position, indicating that the saturation of Mo^{6+} in crystal lattice of TiO_2. With increasing Mo content to 15 %, phase segregated MoO_3 crystals are detected by the XRD peaks at 2θ of 23.42°, 25.70°, and 27.32° in **Fig. 2b**.
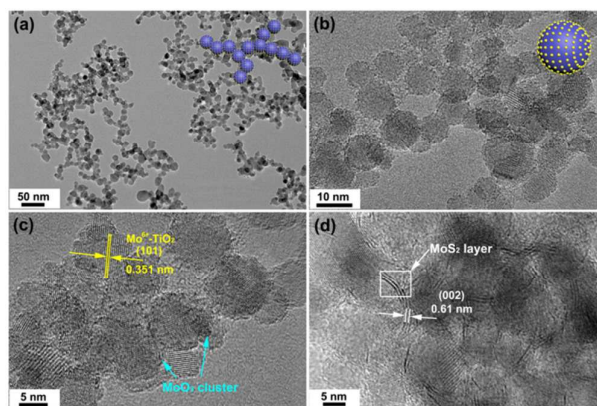

Fig. 3 (a, b) TEM images, (c) HRTEM image of flame made Mo^{6+}-TiO_2/MoO_3 NHs, and (d) HRTEM image of the Mo^{6+}-TiO_2/MoO_3 NHs after the sulfuration with thiourea at 400 °C.

Fig. 3 shows TEM images of flame made Mo^{6+}-TiO_2/MoO_3 NHs. As shown in **Fig. 3a**, the Mo^{6+}-TiO_2/MoO_3 NHs have a diameter in a range of 10-20 nm (SEM image in **Fig. S1**†) and possess a unique particle-particle sintering "neck" to form quasi-chain network structures. The similar morphological structures are also observed for flame made pristine TiO_2 (**Fig. S3**†), indicating the stronger interfacial interaction between particles derived from unique flame temperature gradient. Obviously, compared to a relative smooth surface of TiO_2 particles, the Mo^{6+}-TiO_2/MoO_3 NHs exhibits extremely rough surfaces and lots of ultrafine MoO_3 clusters (less than 1 nm) are homogeneously dispersed on the surface of TiO_2 to form unique core-shell structures, which is demonstrated by TEM images (**Fig. 3b** and **Fig. S2**†). HRTEM image in **Fig. 3c** shows a clear interplanar spacing (0.351 nm) of lattice fringes, which corresponds to the spacing of (101) panes of anatase TiO_2 and indicates the highly crystallinity. The enlarged interplanar spacing (0.350 nm for pure TiO_2) suggests the incorporation of large Mo^{6+} (0.068 nm) into the lattice of TiO_2. This is consistent with the maximum angle negative shifts of 0.08° obtained in the XRD patterns (**Fig. 2b**). The formation of ultrafine MoO_3 species is mainly attributed to a phase-segregation growth after the saturation

of Mo^{6+} doped into TiO_2 lattices during the rapid flame reaction.[28, 30, 31] The corresponding EDX measurement suggests the molar ratio of Mo to Ti is 8.20% (**Fig. S5**†), which is almost close to the designed value of 10%. The Mo/Ti ratio has also been measured to be 9.54% by ICP analysis. With the introduction of more Mo precursor (15 %, ICP measurement: 14.4%), the rough surface on TiO_2 was observed (**Fig. S4**†) owing to the encapsulation of more MoO_3 species, which is in agreement with the XRD results. To further identify the existence of these ultrafine MoO_3 species, the morphology structures of the Mo^{6+}-TiO_2/MoO_3 NHs after the low-temperature sulfuration (thiourea as S sources) are displayed (**Fig. 3d and Fig. S6**†).

Clearly, mono or two MoS_2 layer (a lattice spacing of 0.61 nm corresponds to the (002) plane of MoS_2) are highly dispersed on TiO_2 (weak peak of MoS_2 is also detected by XRD in **Fig. S7**†), suggesting that the existence and highly dispersion of ultrafine MoO_3 clusters. What's more, according to the nitrogen adsorption isotherms measured (**Fig. S8**†), the Mo^{6+}-TiO_2/MoO_3 NHs has a relative high BET specific surface area of 77.6 m^2 g^{-1}, very close to that of pristine TiO_2 (81.9 m^2 g^{-1}) and shows wide pore size in a range of 10 - 100 nm. The formation of these mesopores can be attributed to the agglomerates of quasi-chain NHs and the aggregates of particles, which is demonstrated by the TEM images.
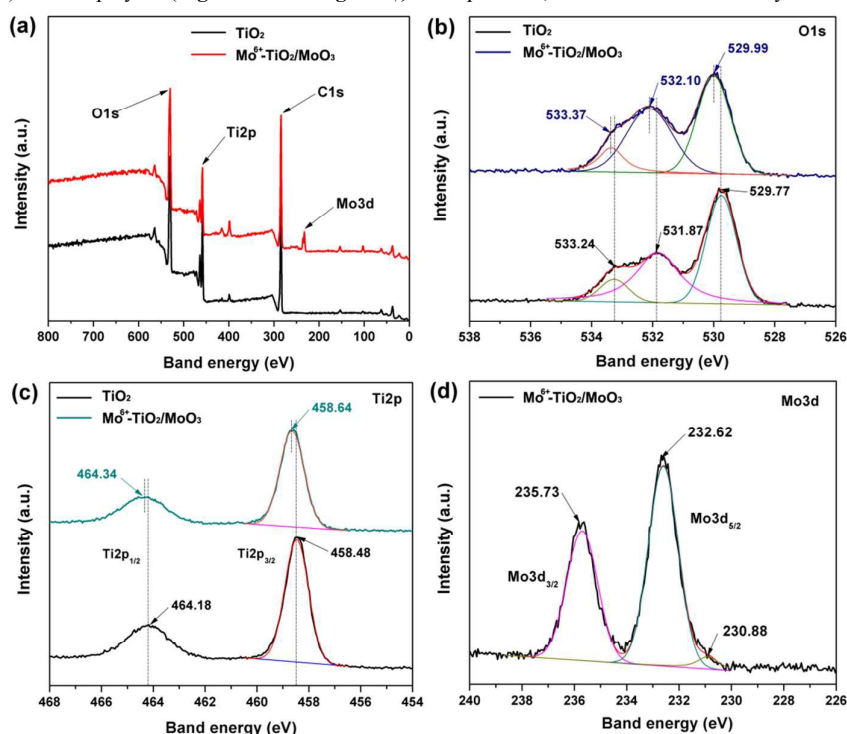

Fig. 4 XPS profiles for pure TiO_2 and Mo^{6+}-TiO_2/MoO_3 NHs: (a) XPS general spectra; (b) O1s; (c) Ti2p; and (d) Mo3d spectra.

For the detailed chemical states of Ti, Mo, O elements, XPS analysis was employed to characterize flame made TiO_2 and Mo^{6+}-TiO_2/MoO_3 NHs. **Fig. 4** depicts the signals of Ti, Mo, and O elements in the XPS spectra. As shown in **Fig. 4a**, additional Mo peaks are clearly observed for the Mo^{6+}-TiO_2/MoO_3 NHs compared to pure TiO_2. **Fig. 4b** shows the O1s XPS spectra of the two materials, which have a similar patterns of three distinct peaks. It is noted that the O1s peaks for TiO_2 are found at 529.77, 531.87, and 533.24 eV, respectively. The peak at 529.77 eV is indexed to the lattice oxygen in TiO_2 and the other two peaks (531.87 and 533.24 eV) can be attributed to the surface hydroxyl group Ti-OH and chemisorbed H_2O molecules. However, for the Mo^{6+}-TiO_2/MoO_3 NHs, the corresponding O1s peaks is found at 529.99, 532.10, 533.37 eV, respectively. A positive shift of 0.22 eV in the binding energy for lattice oxygen is observed compared to the O1s of TiO_2. The O1s could be deconvoluted into two peaks: one at 529.99 eV for the Mo-O bonding and the other one at 529.77 eV for the Ti-O bonding.[25, 34] Furthermore, the $Ti2p_{3/2}$ and $Ti2p_{1/2}$ peaks for the Mo^{6+}-TiO_2/MoO_3 NHs are observed at 458.64 and 464.34 eV,

respectively, as shown in **Fig. 4c**. There is a progressive shift toward higher binding energies than that (458.48 and 464.18 eV) of TiO_2. The binding energy shift (O1s and Ti2p) can be explained by the electron transfer from Ti^{4+} to Mo^{6+} because of the difference in electronegativities of the two metal elements (Mo = 2.16 *vs.* Ti = 1.54).[25] These results indicate the substitutional doping of Mo^{6+} with a higher valence into the TiO_2 lattices and the formation of a Ti-O-Mo linkage. **Fig. 4d** exhibits the Mo3d XPS spectrum and the two peaks at 232.62 and 235.73 eV are identified for the $Mo3d_{5/2}$ and $Mo3d_{3/2}$ patterns, respectively. Moreover, the peak at 230.88 eV suggests that the presence of the Mo^{5+}, which is consistent with the reported Mo^{5+} and Mo^{6+} states inherently in the MoO_3 itself.[34] After the calculation by XPS, the atomic ration of Mo/Ti is 17.4% (more than 10 %), indicating that the phase segregation of ultrafine MoO_3 crystals on the surface of TiO_2, which is demonstrated by the XRD result and TEM observation.

The influence of Mo doping on the electronic structure of TiO_2 crystals are characterized by the UV-visible absorption spectra (**Fig. S9**†). All the samples have similar absorption spectrum in UV region

(< 400 nm) and there is no significant response in the visible light area for the pristine TiO_2 owing to the inherent band gap value of 3.21 eV.[18, 26] However, with the introducing of Mo, the additional absorption band edges show a little red shift to visible region and these samples show an apparent absorption in the wavelength of 400-800 nm compared to that of the pristine TiO_2. The relatively uniform doping of Mo^{6+} is the key to narrowing the bandgap because a new dopant level is formed by introducing some localized states of Mo ions near the conduction band.[26,27] By the calculation, the band

gap value of 3.14, 3.09 and 3.05 eV are obtained for $1Mo-TiO_2$, $5Mo-TiO_2$ and $10Mo-TiO_2$, respectively. The results indicate that Mo ions are successfully incorporated into the lattice of TiO_2 crystals and these dopants create conduction band electrons, oxygen defects or titanium vacancies for the imbalance in the charge, which are beneficial to improve the electrical conductivity of TiO_2 owing to much easier charge transfer.[13, 14, 16-19, 25] The band structures of the TiO_2 and Mo^{6+} doped TiO_2 are also illustrated (**Fig. S9b†**).
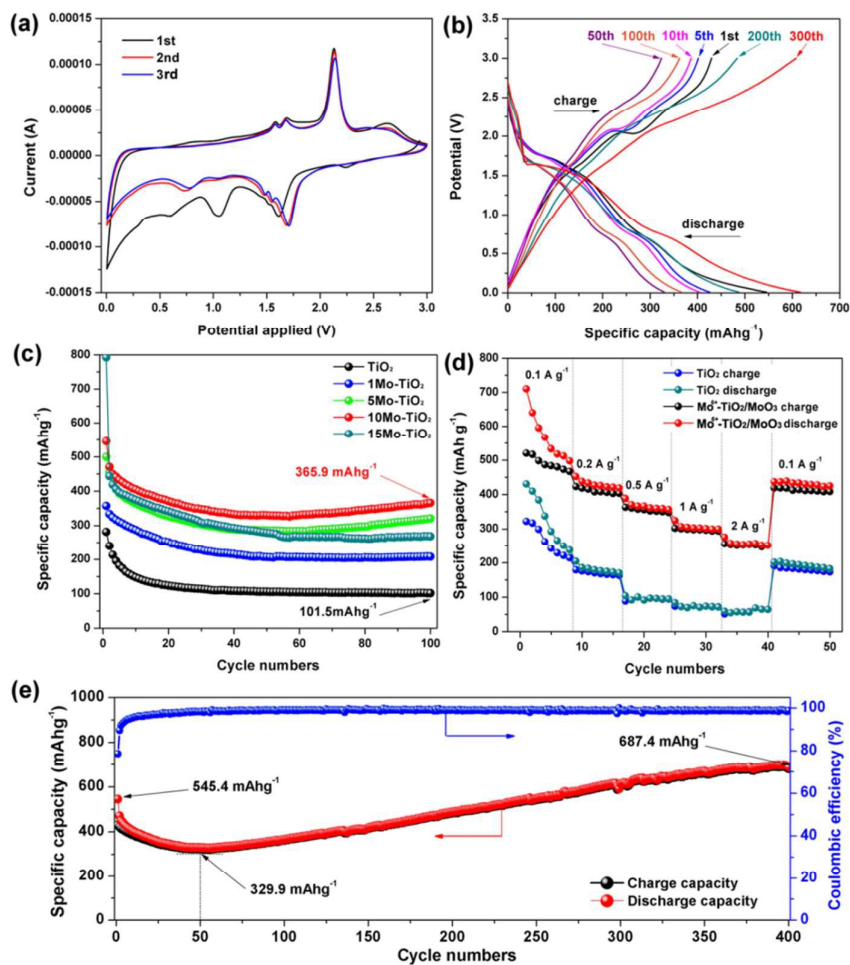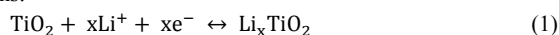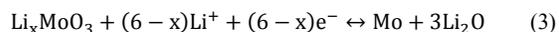

Fig. 5 (a) Cyclic voltammograms of the Mo^{6+}-TiO_2/MoO_3 NHs electrode in the voltage range of 3.0-0.005 V (vs. Li/Li$^+$) at 0.2 mV s^{-1} scanning rate; (b) galvanostatic charge-discharge curves of the Mo^{6+}-TiO_2/MoO_3 NHs anode; (c) cycling performance of flame made TiO_2 with different Mo content at a current density of 0.5 A g^{-1}; (d) rate performance of TiO_2 and Mo^{6+}-TiO_2/MoO_3 NHs at the current density of 0.1, 0.2, 0.5, 1, 2 and 0.1 A g^{-1}, respectively; (e) cycling performance of the Mo^{6+}-TiO_2/MoO_3 NHs electrode at a current density of 0.5 A g^{-1} with 400 cycles.

Electrochemical Performance.

To demonstrate the advantages of the Mo^{6+}-TiO_2/MoO_3 NHs, we investigate these particles' electrochemical lithium storage properties in CR2016 type half-cells. **Fig. 5a** shows the cyclic voltammetry (CV) profiles of the Mo^{6+}-TiO_2/MoO_3 NHs in the voltage range of 0.005 - 3.0 V (vs. Li/Li$^+$) at 0.2 mV s^{-1} scanning rate. In the initial cycle, the obvious oxidation-reduction peaks at 1.61/2.12 V mainly correspond to the Li$^+$ insertion/desertion reaction into TiO_2. In the second and third cycles, the reduction peak for TiO_2 shifts to 1.71 V owing to the further activation process and reduction of the electrode

polarization.[9, 16, 20] Some small distinct potential peaks are observed at 2.23, 1.52, and 1.45 V in the first cathodic scan, indicating the existence of addition type reaction (above 1.25 V) of Li$^+$ ion intercalation to MoO_3 to form Li_xMoO_3 solid solution. In the lower voltage region (below 1.25 V), small peaks in the first cathodic sweep correspond to the initial conversion reduction reaction. The total chemical reaction for Li-ion insertion to/extraction from TiO_2, MoO_3, and subsequent conversion reaction are described as follow equations:[9,16,35,36]

$$TiO_2 + xLi^+ + xe^- \leftrightarrow Li_xTiO_2 \tag{1}$$
$$MoO_3 + xLi^+ + xe^- \leftrightarrow Li_xMoO_3 \tag{2}$$

$$\text{Li}_x\text{MoO}_3 + (6-x)\text{Li}^+ + (6-x)\text{e}^- \leftrightarrow \text{Mo} + 3\text{Li}_2\text{O} \qquad (3)$$

In addition, a small peak observed at 0.29 V relates to the formation of Mo metal species and Li_2O.[36] suggesting that the undergoing of the conversion reaction, which contributes the most capacity. The anodic peaks located at 1.58 and 1.69 V can be assigned to the de-intercalation reaction of Li ions. Moreover, the first scan on the negative-current side have a broad reduction peak in the range of 0 to 1.25 V. Compared with the following scans, these irreversible peaks are mainly attributed to the formed solid electrolyte interphase (SEI) films.[20, 21, 36] These observed peaks further confirmed that the electrochemical reaction takes place in a multistage process with active TiO_2 and MoO_3 components.

Fig. 5b depicts the voltage *vs.* capacity profiles of the Mo^{6+}-$\text{TiO}_2/\text{MoO}_3$ NHs anode for the selected 1st, 5th, 10th, 50th, 100th, 200th and 300th cycles at a current density of 0.5 A g^{-1} between 0.01 and 3.0 V. Initial discharge capacity of 545.4 mA h g^{-1} and charge capacity of 429.4 mA h g^{-1} are obtained respectively, corresponding to 78.7 % coulombic efficiency. After 50 cycles, the reversible capacity have the lowest value of 329.9 mA h g^{-1}. Interestingly, the reversible capacity decreases slowly to 329.9 mA h g^{-1} after 50 cycles, and then increases gradually with cycling and reaches 617.0 mA h g^{-1} after 300 cycles (**Fig. 5b**). However, for the Mo^{6+}-$\text{TiO}_2/\text{MoO}_3$ NHs electrode (15.3 wt% MoO_3 and 84.7 wt% TiO_2), the theoretical capacity could be simply calculated to be 454.6 mA h g^{-1} ($1111 \times 0.153 + 336 \times 0.847 = 454.6$). It is worth noting that this practical capacity of the Mo^{6+}-$\text{TiO}_2/\text{MoO}_3$ NHs surpasses the theoretical value. The similar results are quite common for carbon modified oxides. For example, carbon coated MnO exhibited a much higher capacity of 1268 mA h g^{-1} over the theoretical value of 756 mA h g^{-1} and the MoO_2/C nanosheets had a higher capacity of 1348 mA h g^{-1} than the theoretical value of 838 mA h g^{-1}.[36, 37] As discussed later, the superior lithium storage ability is promoted by

highly dispersed MoO_3 clusters, the doping of Mo^{6+} in the lattice of TiO_2 and nanosized particle-particles sintering interaction.

Fig. 5c exhibits the influence of the flame introduction of Mo species into TiO_2 on lithium storage capacity and cycling performance. The initial discharge capacities of TiO_2, 1Mo-TiO_2, 5Mo-TiO_2, 10Mo-TiO_2 and 15Mo-TiO_2 are 281.7, 357, 499.8, 545.4, and 792.4 mA h g^{-1}, respectively. It is clearly noted that the first discharge capacity gradually increases with the increase of Mo content owing to high theoretical capacity of MoO_3 species. For TiO_2, the discharge capacity decreases to 101.5 mA h g^{-1} after 100 cycles, about 64.0 % capacity loss. In addition, all the samples containing Mo species deliver the better lithium storage capacity than that of pristine TiO_2. Among these electrode materials, the Mo^{6+}-$\text{TiO}_2/\text{MoO}_3$ NHs shows the highest discharge capacity of 365.9 mA h g^{-1} after 100 cycles. Even for the introduction of 1 % Mo species into TiO_2, the enhanced capacity of 208.0 mA h g^{-1} is achieved after 100 cycles, which is twice more than the value of TiO_2 (101.5 mA h g^{-1}, 100 cycles). Obviously, as shown in **Fig. 5c**, the cycle performance shows the similar variation trend that the reversible capacity decreases slowly and then increases gradually with cycling when Mo content exceed 1 %. And more Mo content (15 %) leads to the decreased discharge capacity though there is the highest initial discharge capacity of 792.4 mA h g^{-1}, which may closely relates the dispersion state and size of MoO_3 clusters on TiO_2 particles. Interestingly, after the surface MoO_3 clusters can be converted into highly dispersed MoS_2 layers (**Fig. 3d**), the electrodes exhibit much lower specific capacity of 209.8 mA h g^{-1} than that (365.9 mA h g^{-1}) of the Mo^{6+}-$\text{TiO}_2/\text{MoO}_3$ NHs at 0.5 A g^{-1} after 100 cycles (**Fig. S10†**) owing to a relative low theoretical capacity (~ 600 mA h g^{-1}) of MoS_2 and its increased size compared to MoO_3 clusters after the sulfuration.

Tab. 1 Summary of modified TiO_2 nanocomposites and their lithium ions storage capacity

Materials	Optimal doping	Li-ion storage performance	*References*
Fe_2O_3-TiO_2 nanofibers	N/A	0.01-3.0 V, 0.1 A g^{-1}, 454.5 mA h g^{-1}, 200 cycles	*[41]*
$\text{SnO}_2/\text{TiO}_2$ spheres	N/A	0.01-3.0 V, 0.1 A g^{-1}, 520 mA h g^{-1}, 100 cycles	*[42]*
ZrO_2-TiO_2	Zr/Ti = 1:9	1.0-2.6V, 0.13 A g^{-1}, 160 mA h g^{-1}, 60 cycles	*[43]*
$\text{Co}_3\text{O}_4/\text{TiO}_2$	Co/Ti=9:1	0.01-3.0 V, 0.1 A g^{-1}, 668.0 mA h g^{-1}, 120 cycles	*[44]*
MnO/TiO_2	Mn/Ti=2:1	0.01-3.0 V, 0.1 A g^{-1}, 377.0 mA h g^{-1}, 100 cycles	*[45]*
$\text{MoO}_3@\text{TiO}_2$	Mo/Ti=1:1	1.0-3.0 V, 0.5 A g-1, $\approx$320 mAh/g, 100 cycles	*[46]*
MoO_3-TiO_2 NPs	Mo/Ti=0.42	0.01-3.0 V, 0.06 A g^{-1}, 408 mA h g^{-1}, 200 cycles	*[25]*
Mo^{6+}-$\text{TiO}_2/\text{MoO}_3$ NHs	Mo/Ti=1:10	0.01-3.0 V, 0.5 mA g^{-1}, 687.4 mA h g^{-1}, 400 cycles	*This work*

Fig. 5d shows the rate performance of the Mo^{6+}-$\text{TiO}_2/\text{MoO}_3$ NHs and pure TiO_2 particles at different current densities within the voltage range of 0.01-3.0 V, respectively. In addition to superior capacity and excellent cyclability, the Mo^{6+}-$\text{TiO}_2/\text{MoO}_3$ NHs electrode also exhibits impressive rate performance. The discharge capacity of 497.9 mA h g^{-1} is obtained at a current density of 0.1 A g^{-1} before the 8th cycle. Then the capacity decreases to 419.0, 356.4, 299.7, and 251.5 mA h g^{-1} respectively with the different current density of 0.2, 0.5, 1, 2 A g^{-1} and recovers to 425.0 mA h g^{-1} at a initial current density of 0.1 A g^{-1}. The slow decay of capacity with increasing current density suggests that the Mo^{6+}-$\text{TiO}_2/\text{MoO}_3$ NHs electrode shows an excellent rate performance, especially compared to pristine TiO_2. The enhanced rate capacity properties can be

attributed to the highly efficient Li^+ ions transportation in the quasi-chain NHs structure with particle-particle interaction at nanoscale as well as the superior conductivity and conversion reaction from the internal Mo^{6+} doping and the highly dispersion of MoO_3 clusters. **Fig. 5e** depicts the cycling performance of the Mo^{6+}-$\text{TiO}_2/\text{MoO}_3$ NHs electrode at 0.5 A g^{-1}. The reversible capacity decreases slowly from 545.4 to 329.9 mA h g^{-1} after 50 cycles, and then gradually increases with cycling and reaches 687.4 mA h g^{-1} after 400 cycles. The capacity decrease before 50 cycles can be explained by the formation of SEI layer on the electrode. The increased capacity after 50 cycles can be attributed to the presence of a possible activation process because of the complex composition of MoO_3 clusters and Mo^{6+} ions in the lattice of TiO_2, which is a common for transition

oxides, for example, TiO_2-RGO, Mn_2O_3@TiO_2, TiO_2@SnO_x@C, Fe_2O_3/TiO_2, etc.[38-41] For the hybrid Mo^{6+}-TiO_2/MoO_3 electrode, the complex structures endow them more interfacial interactions, such as the interfaces of doped Mo^{6+} and TiO_2, MoO_3 clusters and TiO_2, and the sintered TiO_2 particles in chain-like structures. It is believed that the complexity of the interfacial reactions results in a longer activation process, which eventually leads the increase of the capacity as the cycling numbers increases. Furthermore, after a few cycles, the coulombic efficiency increases quickly to ~ 100 %. These results demonstrate that the Mo^{6+}-TiO_2/MoO_3 NHs exhibits high capacity and outstanding rate performance, which is superior to the resulted most of TiO_2 based composite electrodes in the literatures, as summarized in **Tab. 1**.
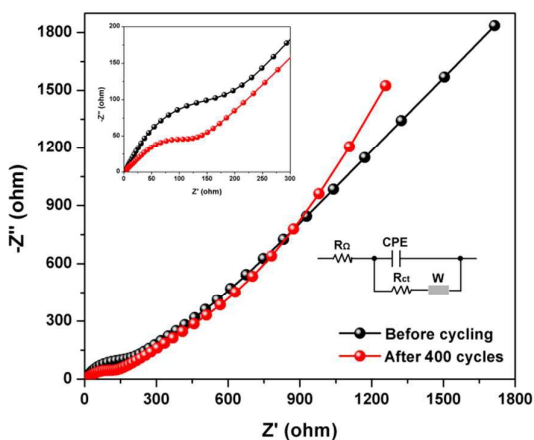

Fig. 6 Nyquist plots of the Mo^{6+}-TiO_2/MoO_3 electrode in the frequency of 0.01 to 10^5 Hz before and after 400 cycles (inset: an enlarged of EIS at high frequency and equivalent circuit).

Attempts to improve the Li^+ ions diffusion kinetics and conductivity of nanostructured TiO_2 have been demonstrated to yield significant enhancements in charge/discharge capacity and rates performance.[13,24,25] To further identify the resistance information of the Mo^{6+}-TiO_2/MoO_3 NHs in LIBs, EIS measurements were carried out over a frequency in a range of 0.01 Hz ~ 10^5 Hz. **Fig. 6** shows the corresponding Nyquist plots (Z' vs. $-Z''$) before and after the 400 discharge-charge cycles. As shown in the inset equivalent circuit, R_Ω refers to the total resistance of the electrolyte, separator, and electrical contacts. R_{ct} corresponds to the charge transfer impedance and the straight line located in the low frequency region is associated to the Li^+ ions diffusion process. Clearly, after 400 cycles, the R_{ct} decreases from 315.5 Ω to 167.8 Ω in Nyquist plots for the Mo^{6+}-TiO_2/MoO_3 NHs anode due to further electrochemical activation.[8, 11, 36]

Based on above results, the superior Li^+ ions storage ability of the Mo^{6+}-TiO_2/MoO_3 NHs could be attributed to the enhanced conductivity from Mo^{6+} doping and unique heterojunctions of TiO_2 and MoO_3 clusters, as illustrated in **Fig. 7**. It is demonstrated that heteroatoms substituted into the TiO_2 lattice can create dopant energy levels and fully modify the electronic structures such as B, N, S, Mn, Ni, and Sn.[13, 18, 14, 17, 24] On one hand, some interstitial oxygen defects and vancancies, or titanium vacancies are created as a result of the difference of ionic radius and electronegatives, which

significantly improves the electrical conductivity and decreases the charge transfer resistance. On the other hand, the doping Mo^{6+} ions with a larger radius (0.068 nm) can induce the increase of unit cell volume in the TiO_2 crystal structure as well as lattice distortion (**Fig. 3c**), which facilitates more Li^+ ions to be inserted into the electrode materials for the high capacity.[14, 17] Furthermore, because of the intriguing temperature gradient in flame, lots of ultrafine MoO_3 crystals are highly dispersed on the in situ Mo^{6+} doped TiO_2 to generate novel heterojucntions by the high-temperature phase-segregation growth and unique sintering effects.[30, 31] As high electrochemical activity components, Mo^{6+} embedded into TiO_2 lattices and highly dispersed ultrafine MoO_3 crystals can provide the extra Li^+ ions storage ability through the conversion reaction (Equation 3). Especially, the Li^+ ions can efficiently react with these ultrafine MoO_3 clusters with an extremely high electrochemical activity for the intercalation and de-intercalation because of more active sites from size effect. The Mo^{6+} ions and MoO_3 clusters provide more extra Li^+ ions storage ability for TiO_2. Moreover, the unique quasi-chain network and intriguing particle-particle interfacial interaction at nanoscale make the electrode have a facilitated pathway for the diffusion and transportation of Li^+ ions and the mixing and wetting with electrolyte and conductive carbon black. These advantages endow the Mo^{6+}-TiO_2/MoO_3 NHs with superior specific capacity and excellent rate performance when employed as anode materials for LIBs.
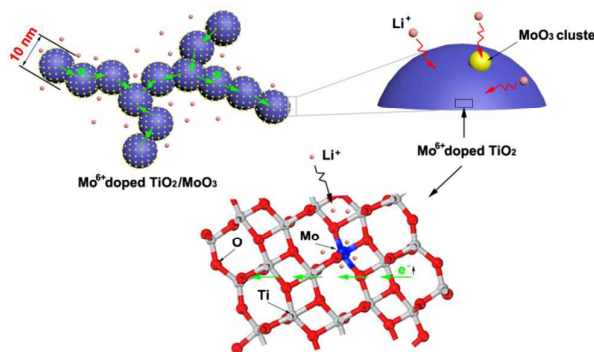

Fig. 7 The illustrated mechanism of the Li^+ ions storage in the Mo^{6+}-TiO_2/MoO_3 NHs.

Conclusions

In summary, internal Mo^{6+} doped TiO_2 nanocrystals *in-situ* decorated with highly dispersed MoO_3 clusters nanohybrids have been realized by a rapid flame spray pyrolysis route for electrochemical energy storage. Such intriguing nanostructures have a primary particle diameter of 10-20 nm, high specific surface area of 77.6 m^2/g, and unique quasi-chain, core-shell structure with particle-particle sintered "neck". With the designed Mo content, Mo^{6+} ions were homogeneously introduced into the TiO_2 host and MoO_3 clusters uniformly *in-situ* dispersed on the surface of doped TiO_2 by the phase-segregation induced growth in spray flame, resulting in the maximization of synergistic effect between TiO_2 and Mo species. When worked as anode materials in LIBs, it is noted that the Mo^{6+} doped TiO_2/MoO_3 NHs display a much higher specific

capacity of ~ 687.4 mA h g^{-1} at 0.5 A g^{-1} even after 400 cycles with superior rate capability of 251.5 mA h g^{-1} at 2 A g^{-1}. The significantly enhancement can be attributed to the improved conductivity from the internal Mo^{6+} doping, extra Li^{+} ions storage spaces from ultrafine MoO$_3$ clusters with highly electrochemical activity and Mo^{6+} ions, and quasi-chain structures with unique particle-particle interfaces. It is expected that aerosol flame process with unique temperature gradient opens a new strategy to design novel hybrid materials by the simultaneous doping and heteroassembly engineering for next-generation LIBs.

Acknowledgements

Notes and references

1   H. Li, Z. X. Wang, L. Q. Chen, and X. J. Huang. *Adv. Mater.*, 2009, **21**, 4593.
2   D. Deng, M. G. Kim, J. Y. Lee, and J. Cho. *Energy Environ. Sci.*, 2009, **2**, 818.
3   G. Q. Zhang, and X. W. Lou. *Angew. Chem. Int. Ed.*, 2014, **53**, 9041.
4   H. Jiang, D. Y. Ren, H. F. Wang, Y. J. Hu, S. J. Guo, H. Y. Yuan, P. J. Hu, L. Zhang, and C. Z. Li. *Adv. Mater.*, 2015, **27**, 3687.
5   B. C. Qiu, M. Y. Xing, and J. L. Zhang. *J. Am. Chem. Soc.*, 2014, **136**, 5852.
6   Z. H. Zhao, J. Tian, Y. H. Sang, A. Cabot, and H. Liu. *Adv. Mater.*, 2015, **27**, 2557
7   X. Y. Yu, H. B. Wu, L. Yu, F. X. Ma, and X. W. Lou. *Angew. Chem. Int. Ed.*, 2015, **54**, 4001.
8   Y. Xu, E. M. Lotfabad, H. L. Wang, B. Farbod, Z. W. Xu, A. Kohandehghan, and D. Mitlin. *Chem. Commun.*, 2013, **49**, 8973.
9   H. Ren, R. B. Yu, J. Y. Wang, Q. Jin, M. Yang, D. Mao, D. Kisailus, H. J. Zhao, and D. Wang. *Nano Lett.*, 2014, **14**, 6679.
10 H. Hu, L. Yu, X. H. Gao, Z. Li, and X. W. Lou. *Energy Environ. Sci.*, 2015, **8**, 1480.
11 R. W. Mo, Z. Y. Lei, K. N. Sun, and D. Rooney. *Adv. Mater.*, 2014, **26**, 2084.
12 T. Xia, W. Zhang, Z. H. Wang, Y. L. Zhang, X. Y. Song, J. Murowchick, V. Battaglia, G. Liu, and X. B. Chen. *Nano Energy*, 2014, **6**, 109.
13 H. J. Tian, F. X. Xin, X. J. Tan, and W. Q. Han. *J. Mater. Chem. A*, 2014, **2**, 10599.
14 W. Zhang, W. D. Zhou, J. H. Wright, Y. N. Kim, D. W. Liu, and X. C. Xiao. *ACS Appl. Mater. Interfaces*, 2014, **6**, 7292.
15 W. Li, F. Wang, Y. P. Liu, J. X. Wang, J. P. Yang, L. J. Zhang, A. A. Elzatahry, D. Al-Dahyan, Y. Y. Xia, and D. Y. Zhao. *Nano Lett.*, 2015, **15**, 2186.
16 Z. H. Bi, M. P. Paranthaman, B. K. Guo, R. R. Unocic, H. M. Meyer III, C. A. Bridges, X. G. Sun, and S. Dai. *J. Mater. Chem. A*, 2014, **2**, 1818.
17 W. Zhang, Y. X. Gong, N. P. Mellott, D. W. Li, and J. G. Li. *J. Power Sources*, 2015, **276**, 39.
18 W. Jiao, N. Li, L. Z. Wang, L. Wen, F. Li, G. Liu, and H. M. Cheng. *Chem. Commun.*, 2013, **49**, 3461.
19 H. Usui, S. Yoshioka, K. Wasada, M. Shimizu, and H. Sakaguchi. *ACS Appl. Mater. Interfaces*, 2015, 7, 6567.
20 D. S. Guan, J. Y. Li, X. F. Gao, and C. Yuan *J. Power Sources*, 2014, **246**, 305.
21 X. Y. Hou, Y. J. Hu, H. Jiang, Y. F. Li, W. G. Li, and C. Z. Li. *J. Mater. Chem. A*, 2015, **3**, 9982.
22 P. Y. Wang, J. W. Lang, D. X. Liu, and X. B. Yan. *Chem. Commun.* 2015, **51**, 11370.
23 C. Y. Yu, Y. Bai, D. Yan, X. G. Li, and W. F. Zhang. *J. Solid State Electrochem.*, 2014, **18**, 1933.
24 H. K. Wang, L. J. Xi, J. Tucek, C. S. Ma, G. Yang, M. K. Leung, R. Zboril, C. M. Niu, and A. L. Rogach. *ChemElectroChem*, 2014, **1**, 1563.
25 J. J. Zhang, T. Huang, L. J. Zhang, and A. S. Yu. *J. Phys. Chem. C*, 2014, **118**, 25300.
26 B. Z. Tian, C. Z. Li, F. Gu, H. B. Jiang, Y. J. Hu, and J. L. Zhang. *Chem. Eng. J.*, 2009, **151**, 220.
27 B. Z. Tian, C. Z. Li, and J. L. Zhang. *Chem. Eng. J.*, 2012, **191**, 402.
28 F. Gu, W. J. Huang, S. F. Wang, X. Cheng, Y. J. Hu, and P. S. Lee. *Phys. Chem. Chem. Phys.*, 2014, **16**, 25679.
29 J. C. Huo, Y. J. Hu, H. Jiang, X. Y. Hou, and C. Z. Li. *Chem. Eng. J.*, 2014, **258**, 163.
30 Y. F. Li, Y. J. Hu, H. Jiang, and C. Z. Li. *Nanoscale*, 2013, **5**, 5360.
31 Y. F. Li, Y. J. Hu, H. Jiang, and C. Z. Li. *CrystEngComm*, 2013, **15**, 6715.
32 Y. F. Li, Y. J. Hu, J. C. Huo, H. Jiang, C. Z. Li, and G. Huang. *Ind. Eng. Chem. Res.*, 2012, **51**, 11157.
33 O. Waser, A. J. Groehn, M. L. Eggersdorfer, and S. E. Pratsinis. *Aerosol Sci. Tech.*, 2014, **48**, 1195.
34 K. Bhattacharyya, J. Majeed, K. K. Dey, P. Ayyub, A. K. Tyagi, and S. R. Bharadwaj. *J. Phys. Chem. C*, 2014, **118**, 15946.
35 X. Li, J. T. Xu, L. Mei, Z. J. Zhang, C. Y. Cui, H. K. Liu, and J. M. Ma. *J. Mater. Chem. A,* 2015, **3**, 3257.
36 P. M. Ette, P. Gurunathan, and K. Ramesha. *J. Power Sources*, 2015, **278**, 630.
37 W. M. Chen, L. Qie, Y. Shen, Y. M. Sun, L. X. Yuan, X. L. Hu, W. X. Zhang, and Y. H. Huang. *Nano Energy*, 2013, **2**, 412.
38 M. M. Zhen, X. J. Guo, G. D. Gao, Z. Zhou, and L. Liu. *Chem. Commun.*, 2014, **50**, 11915.
39 X. Q. Chen, H. B. Lin, X. W. Zheng, X. Cai, P. Xia, Y. M. Zhu, X. P. Li, and W. S. Li. *J. Mater. Chem. A*, 2015, **3**, 18198.
40 Q. H. Tian, Z. X. Zhang, L. Yang, and S. I. Hirano. *RSC Adv.*, 2015, **5**, 40303.
41 H. G. Wang, G. S. Wang, S. Yuan, D. L. Ma, Y. Li, and Y. Zhang. *Nano Res.*, 2015, **8**, 1659.
42 D. Q. Ma, P. Dou, X. H. Yu, H. Y. Yang, H. W. Meng, Y. L. Sun, J. Zheng, and X. H. Xu. *Mater. Lett.,* 2015, **157**, 228.
43 M. V. Reddy, N. Sharma, S. Adams, R. P. Rao, V. K. Peterson, and B. V. Chowdari. *RSC Adv.*, 2015, **5**, 29535.
44 W. T. Li, K. N. Shang, Y. M. Liu, Y. F. Zhu, R. H. Zeng, L. Z. Zhao, Y. W. Wu, L. Li, Y. H. Chu, J. H. Liang, and G. Liu. *Electrochimica Acta*, 2015, **174**, 985.
45 N. Zhao, T. Li, L. Jiao, Y. X. Qi, H. L. Zhu, J. R. Liu, R. H. Fan, N. Lun, and Y. J. Bai. *J. Alloy. Compd.*, 2015, **640**, 15.
46 C. Wang, L. X. Wu, H. Wang, W. H. Zuo, Y. Y. Li, and J. P. Liu. *Adv. Funct. Mater.*, 2015, **25**, 3524.

Nanoscale Accepted Manuscript